Simultaneous Interpretation and Uncertainty Analysis of SCAL Data from Complex Rocks

*Omideza Amrollahinasab, Siroos Azizmohammadi and Holger Ott**

Department Petroleum Engineering, Montanuniversität Leoben, 8700 Leoben, Austria

Abstract

Relative permeability and capillary pressure saturation functions are key uncertainties in reservoir engineering. Many resources are spent on measuring these functions in special core analysis (SCAL) for field developments. Despite the effort and time invested, it is not yet common practice to numerically interpret SCAL data, nor is it common practice to study the resulting uncertainty to reliably extract these two-phase saturation functions. Further developments are particularly important for complex rock types such as microscopically and macroscopically heterogeneous carbonates.

Here, we present a MATLAB-MRST-based simulator for simultaneous matching of SCAL data sets from different experimental techniques. We focus on the most common SCAL techniques, namely, steady-state relative permeability and centrifuge capillary pressure. We discuss the implementation of the common parametrized relative permeability representations and their deficiency to describe data from rather complex rocks such as carbonates. To overcome this limitation, a point-by-point approach is developed and applied to an extensive carbonate data set. For uncertainty analysis, a Markov chain Monte Carlo (MCMC) sampling-based workflow is implemented and applied. The uncertainty is discussed in the frame of the individual data set, simultaneously analyzed data sets, and the sample-to-sample variation, which is an essential step toward stochastic reservoir modeling.

1. Introduction

Dynamic reservoir simulations require relative permeability ($k_r(S_w)$) and capillary pressure ($p_C(S_w)$) saturation functions when immiscible fluid displacement is of concern. Common examples are water flooding for oil production (water/oil), the production of deep geothermal systems (water/steam) and the geological storage of CO_2 (water/CO_2). In these operations, $k_r(S_w)$ and $p_C(S_w)$ decisively dominate the fluid displacement efficiency, sweep efficiency and injection/production pressure. History matching (HM) and predicting reservoir performance by numerical simulations therefore require an accurate input for those saturation functions. Classically, $k_r(S_w)$ and $p_C(S_w)$ are measured in laboratories by core flooding, which is subject to special core analysis (SCAL).

In SCAL, relative permeability is measured by the flooding experiments e.g. steady-state (SS) method, in which the two fluid phases, e.g., oil and water or CO_2 and water, are injected simultaneously at a constant total injection rate and at a certain fractional flow. By measuring the differential pressure and the water saturation after reaching steady-state conditions, Darcy's law can be used to calculate the relative permeability at that fractional flow point, and the scanning of the fractional flow curve allows us to measure the entire relative permeability curves. However, typically, the measured differential pressure cannot be assigned to a single S_w, since capillarity influences the fluid distribution in the rock—the so-called capillary end effect—$k_r(S_w)$ and $p_C(S_w)$ are coupled [1, 2]. Furthermore, in flooding experiments, the saturation endpoints are typically not reached in a finite time. Toward endpoints, relative permeability measurements are often extended by other experimental methods, such as single-speed centrifuge experiments. In these examples, it turns out that single measurements may not describe a saturation function sufficiently, which means that measurements and analyses need to be combined. This is due to the natural inference of $k_r(S_w)$ and $p_C(S_w)$ in any type of two-phase flow experiments. For this reason, the classic analytical solutions to the SCAL experimental methods, such as using Darcy's law for SS, JBN analysis [3] for un-steady state (USS), and Hassler–Brunner [4] and Hagoort's [5] approaches for the analysis of centrifuge measurements, fail, as does the numerical description of individual data sets [6].

By numerical data interpretation, the full physical picture can be considered by a subsequent interpretation of $p_C(S_w)$ and $k_r(S_w)$ experiments or by a simultaneous interpretation of data sets [7, 8]. The latter case does not refer to the best match of the individual data set but to the best combined description, leading to a robust and reliable interpretation. Numerical SCAL interpretation refers to the inverse modeling approach, in which the simulation results are iteratively matched to the experimental data. However, inverse modeling is an ill-posed problem with intrinsic uncertainties [9]. Non-uniqueness and instabilities in part are the results of weighting assigned in the objective function, averaging methods applied and experimental uncertainties such as instrumental noise and systematic errors. It is also not necessarily given that the underlying physical model is sufficient to describe experimental observations. Examples may be simple, e.g., sample heterogeneity that is typically not accounted for in

SCAL interpretation, and pressure and saturation fluctuations by ganglion dynamics are not represented in the modeling approach using Darcy's law [10, 11]. Additionally, the restriction to certain parametrized representations of $p_C(S_w)$ and $k_r(S_w)$, such as the Brooks Corey [12], modified Corey [13] or LET [14] representations, may be a threat for the interpretation of complex rocks such as carbonates [9]. As a result of this discussion, single representations of p_C and k_r saturation functions may not be sufficient for reliable reservoir flow predictions; uncertainty intervals should be included in modern stochastic reservoir modeling. The first promising attempts in this direction have been made in [9, 11, 15]. However, neither numerical interpretation nor uncertainty modeling is yet common practice in SCAL interpretation. A reason may be that the sophisticated SCAL simulation tools are proprietary, which hinders developments in this area.

With this paper, we provide an MRST-based open-source simulator running in MATLAB, for a comprehensive interpretation of SCAL experiments. The work focuses (a) on uncertainty modeling and probabilistic analysis following a Monte Carlo type of sampling with the goal of obtaining realistic intervals for early decision making and stochastic reservoir modeling. (b) Saturation functions are optionally constructed differently from common representations, depending on the complexity of the rock type under investigation. For the interpretation of rock types with a high complexity (the majority of carbonates), we introduce an optional point-by-point approach, which does not follow a specified mathematical function. With this approach, we overcome the limitations of the classic parametrization, which is demonstrated and discussed on a complex carbonate. The simulator runs forward simulations with the MATLAB Reservoir Simulation Toolbox (MRST) [16]. The gradient-based history matching used the MATLAB optimization toolbox. We also employed parallel high-performance delayed-rejection adaptive-metropolis Markov chain Monte Carlo (MCMC) (ParaDRAM) [17], all of which are open-source toolboxes built in MATLAB.

2. Experimental Materials and Methods

SCAL experiments were performed on Estaillades limestone, a rather complex, dual porosity carbonate rock type. The SS and centrifuge (CF) data were published in [18]. The data set represents a primary drainage process on the original water-wet state of the rock.

Rock Samples: Experimental results from 5 rock samples taken from the same outcrop block of Estaillades limestone are discussed in this paper. The average porosity was determined to be ϕ~0.28, and the average permeability was determined to be K~164 mD. The sample properties are summarized in Table 1. The block showed overall porosity variations of 10% and permeability variations of 28% [18].

Table 1: Rock samples, rock properties and experimental process.

Sample ID	Porosity (fraction)	Permeability (mD)	Measurement
1	0.293	142.3	Steady-state relative permeability; primary drainage
2	0.271	141.8	
3	0.283	204.1	Multispeed centrifuge capillary pressure; primary drainage
4	0.283	141.2	
5	0.274	189.8	

The rock type was of dual porosity with a pure calcite mineralogy [18]. The samples were drilled and cut to dimensions of 3.75 cm diameter and 5 cm length for both types of experiments. Subsequently, the samples were cleaned, and $S_w = 1$ was established as the starting point for the drainage experiments.

Fluids: The SCAL experiments were performed at ambient pressure and temperature conditions (22 °C) using brine and decane as wetting and nonwetting fluids. The brine contained 3 wt% NaCl and 5 wt% CsCl as X-ray doping agents. Under experimental conditions, the brine viscosity was measured to be 0.993 cP, and the viscosity of decane was measured to be 0.827 cP.

Steady-State Experiments: Primary drainage SS relative permeability experiments were performed in vertical geometry by simultaneously injecting oil and water from top to bottom. The total injection rate was kept constant at 3 ml/min at different water fractional flow (f_w) steps.

The samples were initially saturated to S_w =1 under vacuum conditions, followed by the first SS measurement at f_w =1, delivering the absolute permeability. f_w was then stepwise decreased by keeping the total flow rate constant. For each f_w step, the differential pressure and the 1D saturation profile along the core were measured after reaching steady state.

The differential pressure was measured in two ways: (a) from injection to production end over the total porous domain (the data shown here) and (b) locally, over a length of 2.5 cm around the center of the plug over which the saturation profile was essentially flat (to exclude the capillary end effect). The local measurement allows us to analytically calculate the relative permeability point-by-point using Darcy's law. The analytical solution serves as an initial guess for numerical interpretation. The saturation was monitored by measuring the X-ray attenuation profile along the core, which is sensitive to different X-ray absorption coefficients of the fluids and hence to the saturation state.

Multispeed Centrifuge Experiments: Centrifuge experiments were performed in drainage mode, starting from S_w =1, established in the same way as for the SS experiments. The samples were desaturated in multiple steps of increasing centrifugal acceleration and angular frequencies. During the experiment, the cumulative water production was recorded by an automatic stroboscopic read-out system. At the end of each experimental step no further water production was observed. From the cumulative water production, the average water saturation ($\overline{S_w}$) can be calculated. From $\overline{S_w}$ and the centrifugal

acceleration, $p_C(S_w)$ can be estimated by the Hasser–Brunner equations [4], which serve as a starting point for the numerical data interpretation further below.

3. Numerical Methods and Implementation

The forward modeling part is using the MRST to simulate the SS, unsteady-state (USS), and CF experiments both in an imbibition and drainage mode. We use the term "forward modeling" for the case in which we have the full set of rock and fluid properties available, and we numerically simulate SCAL experiments. Forward modeling is especially useful to design experiments and for quality control purposes of, e.g., third-party data, or to judge the validity of analytical solutions as starting point for numerical analysis; typically, analytical solutions serve as starting points of the numerical workflow.

The initial step in our methodology begins with calculating the saturation functions from the experimental measurements using the corresponding analytical solutions, i.e., the Darcy equation for SS experiments and the Hassler–Brunner equations [4] for CF experiments. Then, we implement an objective function with which we search for the least mean square error between the experimental measurements of the SS (pressure and saturation profiles) and CF experiments (average water saturation) and the corresponding simulation predictions. These errors are summed up in a single total error to be able to match both experiments simultaneously. This objective function is then fed into the MATLAB optimization toolbox *fmincon* function.

The *fmincon* function attempts to optimize the saturation functions by minimizing the least mean square error defined in the objective function. The variation in the saturation functions is done in a point-by-point fashion to overcome the limitations of saturation function parametrization functions, e.g., Corey [12] and LET [14], which is further explained in the section on the parametrization of saturation functions. The results of the history matching simulation are then input into the *ParaDRAM* package to run the Monte Carlo simulations, sampling variations of the saturation tables in the vicinity of the history match results, and quantify the uncertainty ranges around the history-matched solution.

As far as the convenience of use and the computational efficiency are concerned, MRST serves our purpose. Details, especially on the latter, are discussed further below.

Flow Equations and Solver: For the simulation of SCAL experiments, immiscible and incompressible fluid phases are assumed. Furthermore, fluid viscosities are assumed to be pressure independent and can be specified by the user. Under these conditions, two-phase flow can be described by the following governing equations: in the absence of source and sink terms, the material balance is expressed as:

$$\phi\, \partial_t(S_\alpha) + \nabla \cdot (\overrightarrow{v_\alpha}) = 0 \qquad \alpha = w, o \qquad (1)$$

Here, ϕ is the porosity and S_α is the phase saturation—both dimensionless—and $\overrightarrow{v_a}$ is the Darcy phase velocity vector in units of m/s. Without the restriction to a specific combination of fluids we refer the two phases α to oil (o) and water (w) in the following. The Darcy velocity $\overrightarrow{v_a}$ is given by Darcy's law:

$$\overrightarrow{v_\alpha} = -\left(\frac{k_{r\alpha}}{\mu_\alpha}\right) K(\nabla p_\alpha - \rho_\alpha \vec{g}) \qquad \alpha = w, o \qquad (2)$$

where $k_{r\alpha}$ are the dimensionless relative permeability saturation functions and μ_α are the phase viscosities in Pa · s. K is the absolute rock permeability in m^2, p_α are the phase pressures in Pa, and g is the gravitational constant in m/s^2. Furthermore, the phase saturations satisfy $S_w + S_o = 1$, and incompressible flow is further restricted to $\nabla \cdot (\overrightarrow{v_w} + \overrightarrow{v_o}) = 0$.

The solver is based on the MRST automatic differentiation (AD) toolbox, including differentiation and divergence operators, automatic differentiation to compute the Jacobians, object-oriented framework, and state functions from which we make use in the simulator. The details on how these operators are implemented in the MRST framework can be found in [19].

The simulation time and the desired time stepping are managed by using the MRST *rampupTimesteps* function, which increases the simulations' stability and accuracy since there are usually relatively larger changes in the saturation and pressure at the beginning of a simulation schedule. Then, the *simulateScheduleAD* function is used for simulations using fully implicit formulation and adaptive time step adjustments in case of convergence failures.

For the carbonate rock simulations shown in this paper, a maximum time step of ~20 hours with ~10 geometrically ramped-up time steps show the best tradeoff between the accuracy and the simulation speed for most of the cases.

Parametrization of Saturation Functions: SCAL data are numerically calculated by varying $k_r(S_w)$ and $p_C(S_w)$ to be compared with the experimental measurements e.g. pressure and saturation measurements. Traditionally, these saturation functions are constructed using parametrized power law functions. These functions are partly physically motivated [12] and partly designed to allow an effective description of a wide range of rock types [14]. The disadvantage of power laws is that they generally constrain the shape of the resulting saturation function. They also impact the history matching process, as they may cause highly non-unique response surfaces of the objective function that the optimizer is trying to minimize [9].

In this work, saturation functions are constructed point by point since a higher flexibility was needed to describe the specific carbonate rock type. In the point-by-point approach, we interpolate linearly between adjacent points using the MRST *interpTable* function. Derivatives are then computed by the piecewise linear interpolant. To find the overall best match of $k_r(S_w)$ and $p_C(S_w)$, the SS and multispeed CF data sets are interpreted pairwise and simultaneously. The saturation points are chosen on the basis of the experimental average water saturations after steady conditions were reached. The achieved saturation ranges of the individual data sets may be different. In the present case of primary drainage, S_{cw} may be reached by CF but typically not by SS. Therefore, outside the SS

saturation range, k_r is sensitive only to the CF measurement. The average of the saturation profiles at each fractional flow from SS defines the middle range water saturations, and the average water saturation from CF experiment defines the lower water saturations. In this way we define the water saturation vector on which the history matching process is performed. For simultaneous evaluation of $k_r(S_w)$ and $p_C(S_w)$, the MATLAB *fmincon* function automatically scales the input parameters to assist the optimization process. However, during the uncertainty quantification using the ParaDRAM package, no input parameter scaling is applied. To date, the point-by-point approach has not caused any numerical stability problems.

Steady-State and Unsteady-State Model: Steady-state and unsteady-state core flood experiments are modeled in a 1D linear domain as displayed in Figure 1 using the *tensorGrid* function in *MRST*. The domain size is adapted to the dimensions of the rock samples and regularly discretized in the flow direction with a grid size of 1 mm. This gridding scheme is inspired from the work of [6]. As typical in SCAL, the domain is considered homogeneous in all rock properties and is populated with the experimentally determined average values for K and ϕ.

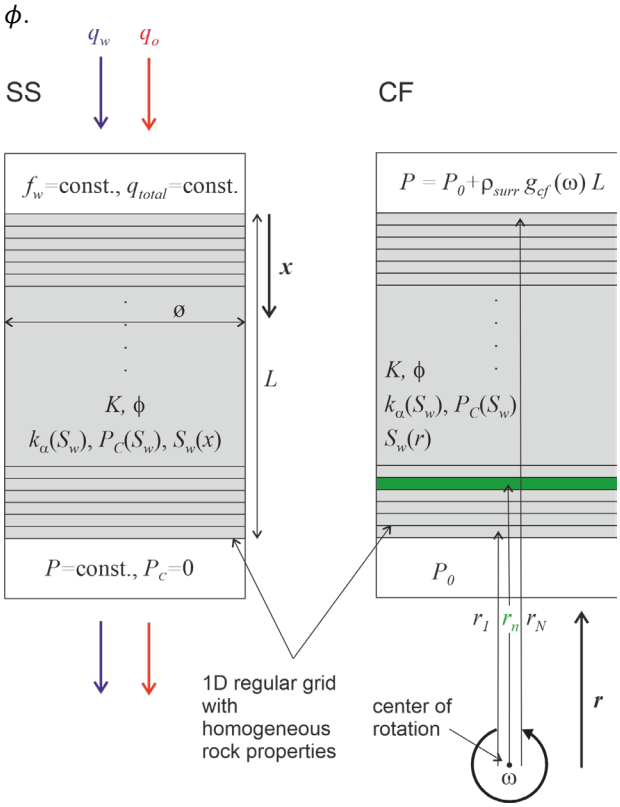

Figure 1: Modeling domains for matching steady-state (SS, left) and centrifuge experiments (CF, right). In this figure, f_w is the fractional flow of water, q_{total} total injected flow rate, ϕ porosity, P_C capillary pressure, K the absolute permeability, S_w water saturation, and P_0 initial pressure.

Extra grid blocks with the same volume are added to either end of the simulation domain to apply the inlet and outlet boundary conditions. By assigning $\phi = 1$, $P_C = 0$, and straight-line k_r functions, the discontinuity at the inlet and outlet boundary is introduced [6]. The experimental boundary conditions are also applied to these extra grids; at the inlet boundary cell, constant flow rates, and at the outlet, constant pressure boundary conditions are applied by using the *fluxside* and *pside* functions in the *MRST*. The differential pressure is calculated as the pressure difference between the boundary cells at each end of the core. Since we assume the capillary pressure in these boundary cells to be zero, the water and oil pressures are the same in both cells, and the reported differential pressure applies to the respective connected fluid phase in the domain. For the calculations of average water saturations, these boundary cells are omitted from the water saturation profile outputs since the boundary cells are not a part of the main core body.

For the initialization of the primary drainage processes, the water saturations in the inlet and outlet boundary cells are set to one, and for the first imbibition process, they are set to zero. These settings follow the experimental layout, with the experiments starting at $f_w = 1$ for drainage and at $f_w = 0$ for imbibition.

By realizing the boundary conditions as described referring to the experimental settings of the injection pumps and the backpressure system, the experimental responses can be modeled and compared to the actual measurements. These are the differential pressure as measured by pressure transducers and the 1D saturation profiles, which are determined by X-ray absorption measurements.

Multispeed Centrifuge Model: For modeling centrifuge experiments, the modeling domain is set up as for the SS and USS core flood experiments. However, the driving force refers to the gravity term in equation (2). The model geometry is given on the right side of Figure 1. In centrifuge experiments, gravity is applied by centrifugal acceleration $g_{cf} = \omega^2 r$, in which r denotes the distance from the center of rotation; therefore, gravity varies along the modeling domain, i.e., along the core sample.

For the simulations of an individual experimental step at a constant angular frequency ω, both ends of the core are assigned a constant pressure boundary condition. The pressure boundary conditions in CF experiments are governed by the hydrostatic pressure in the surrounding fluid that invades during the CF experiment. At the boundary toward the center of rotation, the pressure is set to a constant $P_0 = \rho_{surr}\omega^2 r_0$, while on the opposite side of the modeling domain, the gravitational head amounts to $P = \rho_{surr}\omega^2 r_{N+1}$, with r_0 and r_{N+1} being the positions of the two boundary grid blocks and ρ_{surr} being the density of the surrounding/invading fluid, which is oil in the case of drainage and water in the case of an imbibition process. Defining the boundary conditions as above allows us to establish the surrounding hydrostatic pressure and naturally account for the gravity-induced fluid flow in and out of the modeling domain.

A centrifuge device requires a certain time to reach the predefined angular velocity, which is called the startup time. This startup period affects the production profile, especially from cores with high absolute permeability. In the simulator, to account for the startup period we divide the startup rotation per minute (RPM) to the startup time and assume a linear increase in the centrifuge RPM to calculate a maximum rate at which the centrifuge RPM

can change over time (in the units of RPM/s). Then we scan through the CF rotation schedule and break it down into smaller RPM increase steps based on the maximum rate that the CF RPM can change. In the simulations, a startup period of 100 s to 2000 rpm is assumed, discretized in five 20-second steps.

4. History Matching

SCAL data interpretation by numerical history matching is well established but not yet common practice. A best practice is an assisted history matching procedure based on a user-defined objective function to be minimized, which also allows for a subsequent uncertainty analysis [9]. In this work, we go two steps beyond: first, similar to [20, 21], we analyze data sets of different measurements simultaneously instead of subsequently. Simultaneous analysis facilitates finding the best combined match of $k_r(S_w)$ and $p_C(S_w)$ by minimizing a common and normalized objective function. Second, in numerical HM, the $k_r(S_w)$ and $p_C(S_w)$ functions are typically represented by power laws, which is physically expected for simple rock types [13] [12]. The present module also allows a point-by-point description of $k_r(S_w)$ and $p_C(S_w)$ to match experimental data from highly complex rock types without the limitations of specific power-law representations.

In general, numerical HM is an underdetermined process, for which the Levenberg–Marquardt algorithm is used because of its robustness to the starting values [21] [22]. However, in contrast to the Levenberg–Marquardt approach, the *MATLAB fmincon* function implements interior-point or active-set algorithms in which a constrained nonlinear optimization algorithm allows for the implementation of inequalities; inequalities are essential for the aspired point-by-point approach to enforce monotonic behavior of k_r and p_C saturation functions, which is naturally the case by power-law representations. Monotonicity is demanded from a physical point of view, since we do not expect that, e.g., the phase permeability decreases with increasing saturation.

Inside the *fmincon* function, we set the optimization algorithm to be the *active set,* as it provides the best possible results by minimizing the following objective function:

$$K = \frac{1}{N_{obs}} \sum_{i=1}^{N_{obs}} \left(\frac{d_i - y_i}{d_i}\right)^2 \qquad (3)$$

where d_i are the observed experimental values, y_i are the simulated responses, and N_{obs} is the number of parameters, which is equal to the number of measured data points. Various objective functions are reported in the relevant literature [11]. The convergence criteria for the *fmincon* function is the default 10^{-6} difference between the two last calculated objective function values. The χ^2 function is most commonly used as objective function for history matching purpose, however we found equation (3) to be more suitable for the simultaneous history matching of SS and CF experiments and point-by-point representation of the saturation tables. Simultaneous experiments affect the data that we are matching (causing a different error surface) and the choice of representation affects the points that we are iterating on. This is because the measurements are at different scales (i.e., numerical values) and at different resolutions (i.e., point density), which is accounted for by the well-normalized objective function in equation (3). The available analytical solutions serve as a starting point for the HM process, which ensures that the solution is close enough to the optimal solution to minimize the chances of approaching a local minimum instead of the optimal solution.

4.1 Uncertainty modeling

After finding a match between the experimental and numerical responses, we explore the response surface around our optimal solution and determine its sensitivity. As also shown by [9], the history matching problem is ill-posed with local minima. In such cases, solutions through a Hessian matrix and a χ^2 analysis may fail. Instead, we opt for MCMC sampling.

In the traditional MCMC methods, manual tuning of parameters within the sampling algorithm may be required to ensure the convergence of the Markov chain to the target densities for the problem at hand. To avoid manual tuning, we use the ParaDRAM library, which offers a practical implementation of the delayed-rejection adaptive-metropolis MCMC or DRAM algorithm. DRAM is fully automated regarding the selection of the free parameters and is an extension of the traditional Metropolis–Hastings (MH) method [17].

The DRAM algorithm combines two algorithms, namely, the delayed-rejection (DR) and adaptive-metropolis (AM) algorithms. The AM algorithm, as opposed to the MH algorithm, adapts the proposal distribution based on the past history of the Markov chain (the points sampled thus far), and the DR algorithm improves the efficiency of the MCMC sampler, especially in higher dimensional problems; in high-dimensional domains, the number of rejections can become more significant than the acceptance, strongly compromising the efficiency of the sampler. Therefore, DRAM can be useful since the point-by-point construction of saturation functions refers to a high-dimensional space. Furthermore, this method is particularly useful for multimodal target density functions separated by deep valleys of low likelihood. Therefore, in the case of multiple local minima in the objective function response surface, this method can help us find them [23].

The MatDRAM algorithm [23] (existing in the ParaDRAM library) offers a practical variant of the generic DRAM algorithm relaxing the requirements for (a) a set of delayed-rejection-stage proposal distributions and (b) reduces the complexity of the acceptance probability. Symmetric proposal distributions with a fixed shape are used through the DR process, and the scales are determined through a user-defined schedule. To run the MCMC simulations, we use a likelihood estimation function as follows:

$$J = \frac{1}{N_{obs}} \sum_{i=1}^{N_{obs}} -\frac{1}{2} \left(\frac{d_i - y_i}{error \cdot d_i}\right)^2 \qquad (4)$$

where $error$ is a fixed value between 0 and 1 (expressed as a percentage below) and we multiply -1/2 to this function since here we aim to maximize the probability rather than minimizing as in equation (4). We assume a relative error of 2.5% for the pressure reading, 1% for the saturation profile of SS experiments, and 1% for the average water saturation of CF experiments. These fixed error values are simple assumptions coming from the experimental measurements' average standard deviation after steady state was reached. The experimental measurements act as observed (true) values, and through ParaMonte iterations, J is calculated from simulation predictions. During the MCMC simulations, $k_r(S_w)$ is hard bounded between zero and one, and $p_C(S_w)$ bounds are set to be half and double the optimum values (the minima – or the best saturation function - which is found in the history matching simulations) as lower and upper boundaries.

To force a monotonic behavior of the point-by-point saturation functions, we define a prior inequality function that checks if:

$$Ax \leq b \tag{5}$$

Where x is a vector, containing the parameters that are history matched, and the matrix A and vector b are defined in a way to have:

$$x_i \leq x_{i+1} \text{ or } x_i \leq x_{i-1} \tag{6}$$

based on the type of monotony that is forced on the parameters. This inequality is run before the likelihood estimation above (equation (4)), and if it is not valid we reject the sample before running the simulations to save computational time. In this function, we create the A and b matrix, in the same way the inequalities are forced in the MATLAB optimization toolbox [24], and reject the samples that are not monotonic prior to our main likelihood estimation function. This method saves computational time by not rejecting samples without running the main likelihood estimation function.

5. Benchmarking and Verification

The model's accuracy was verified by using synthetic data sets published by Lenormand et al. [25] and Loeve et al. [8] for the forward modeling and history matching modules, respectively. The simulator has been benchmarked with 5 simulation cases to the results of accepted SCAL simulators by comparing the results to [25]. Figure 2 shows (a) the $k_r(S_w)$ and (b) the $p_C(S_w)$ input and the comparison with the differential pressure and saturation data simulated by the SCORES simulator expressing $k_r(S_w)$ with a Corey model and $p_C(S_w)$ as tabulated values. Case 1 (c) represents the differential pressure during SS imbibition in a neutral-wet system.

The synthetic data set includes bump floods as typically performed at the end of SS experiments to increase the accessible saturation window. Figure 2 (d) refers to a water-wet primary drainage process and the respective average water saturation from a CF experiment.

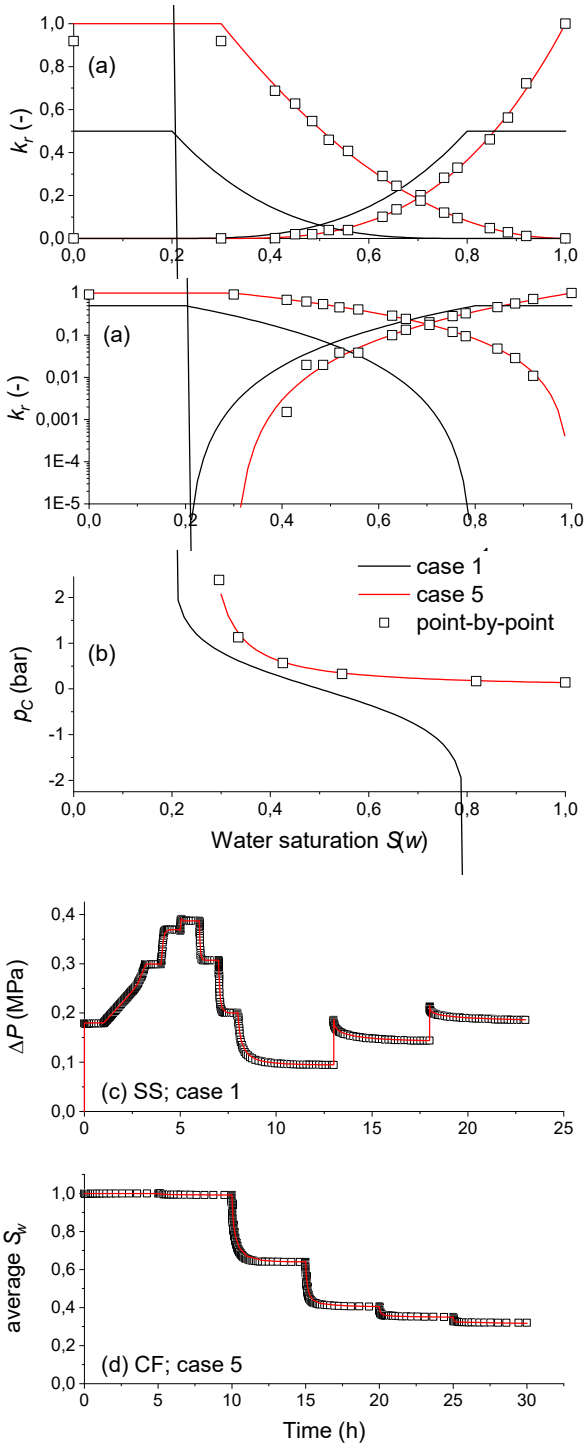

Figure 2: Verification by forward simulation using the reference data set presented by *[25]*. (a) and (b): Relative permeability and capillary pressure saturation functions, respectively, for primary drainage (case 5) and first imbibition (case 1). Panels (c) and (d) show the forward simulated differential pressure from SS (case 1) and the simulated average water saturation of the CF experiment of case 5, respectively. The symbols are simulated with SCORES, and the lines correspond to the simulator developed in the present work. The open squares in (a) and (b) refer to point-by-point matches of forward simulated experimental responses.

All simulation results show perfect agreement between all simulators, including the one developed in this work. For case 1, a domain discretized into 80 grid cells and a

maximum time step of 0.2 h lead to a runtime of ~16 s using a 9th series core i7 Intel CPU. For this benchmark we use *simulateScheduleAD* with the default parameters – fully implicit scheme and *LinearSolverAD* that calls standard MATLAB direct solver mldivide.

To benchmark the HM module and to demonstrate the MC uncertainty quantification, we use the synthetic data set by [8] to simultaneously match an USS and multi-speed CF imbibition experiment. The data set consists of unsteady-state (USS) and multispeed centrifuge simulated calculations (the synthetic pressure and production data). The Corey-type $k_r(S_w)$ [12] and the Skjaeveland-type [26] $p_C(S_w)$ input functions are shown in Figure 3 (a) and (b). The upper and lower bounds as well as the starting point of the HM are chosen as in [8]. The results are shown in the same panels. Deviations from the true values are found at connate water saturation and the oil endpoint relative permeability. The reason may be the limited information an USS imbibition experiment delivers at low water saturations. The uncertainty analysis is performed by assuming a 2.5% relative error for the pressure and production responses. Figure 3 (c) shows the resulting histograms and the two-parameter correlations for the relative permeability functions. On the contour plots, the Pearson's correlation strengths are given in addition to red numbers [27]. Strong correlations are found between the endpoint relative permeability and endpoint saturations of the complimentary phase, as evident in the Pearson's correlation matrix. The endpoint relative permeability also shows a strong correlation with the respective Corey exponents. This is a property of the specific mathematical representation of the saturation functions. For example, a change in the oil Corey exponent directly modifies the oil endpoint relative permeability at a given connate water saturation. The correlations may also provide a physical interpretation as far as the used function is physically motivated.

Above, the classic power-law representations are used to history match (HM) the synthetic datasets and benchmark the SCAL simulator HM module. In the point-by-point representation of the saturation functions, how many free history-matching parameters we have is determined by the count of the fractional flow steps implemented in the SS experiment, and the count of different rotational speeds implemented in the CF experiment. We use the $k_r(S_w)$ and $p_C(S_w)$ of [25] case 5 as input to simulate the primary drainage SS and CF experiments with 12 SS fractional flow (f_w) steps and 5 CF centrifugal speed steps. The simulated experimental responses are then matched with the point-by-point approach using the analytical solutions as starting points. The resulting saturation curves are shown as scatter graphs in Figure 2 (a) and (b). Naturally, the solution shows a certain scatter but describes the input saturation functions well. Deviations are found at the oil endpoint k_r. This may be expected since the SS drainage does not reach true S_{wc} and the centrifuge is missing sensitivity to k_r of the invading phase at that point.

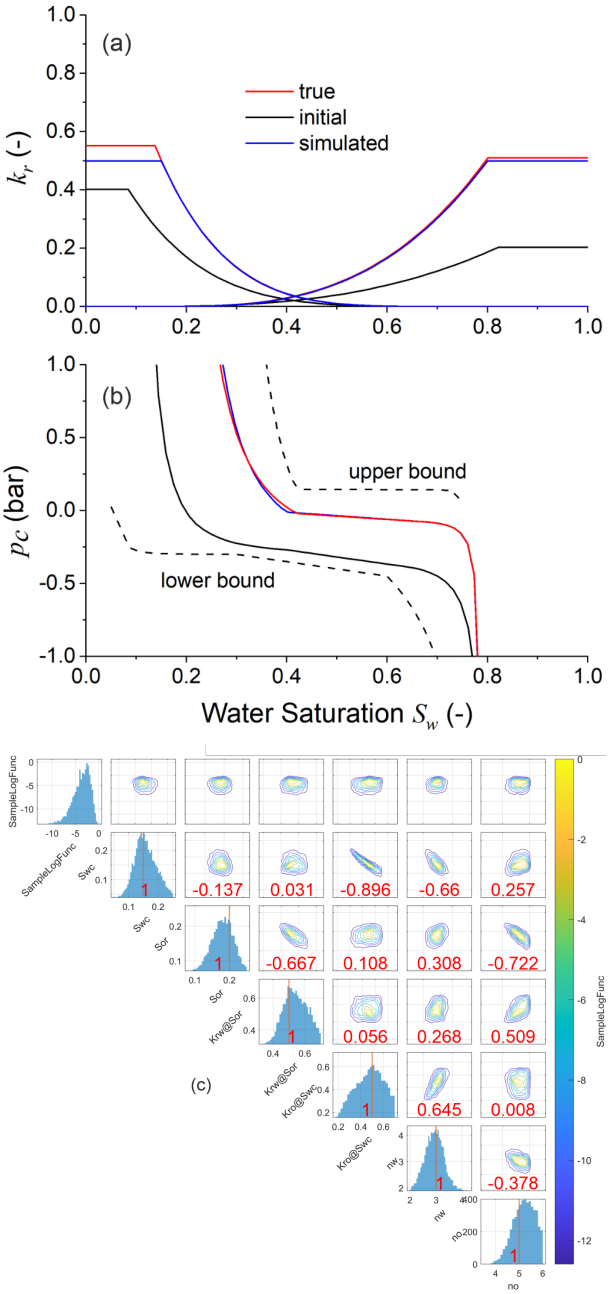

Figure 3: Simultaneous history matching and uncertainty quantification for benchmarking. Synthetic data sets of an unsteady-state and a multispeed centrifuge experiment *[8]* are matched with modified Corey and Skjaeveland parametrizations. True values, starting points and the matches are shown in (a) for relative permeability and (b) capillary pressure (see text for details). (c) shows the result of the MCMC uncertainty analysis. The diagonal shows the single parameter probability distribution (histograms). The off-diagonal elements (contour plots) show the two-parameter correlations for the relative permeability curves. The red numbers refer to the Pearson correlation strength matrix.

6. Results

The real case study is performed on an SCAL data set of Estaillades limestone. The data set consists of two steady-state primary drainage relative permeability measurements and three multispeed centrifuge experiments. The experiments have been pair-wise simultaneously matched. Data from a CF/SS combination (samples 2 and 5) are shown in Figure 4. Details about the rock type and rock properties of the individual plugs are summarized in the Materials and methods section above.

At first, we simultaneously matched CF (average water saturations) and SS (pressure and saturation profiles) experimental measurements by using various power-law representations for $k_r(S_w)$, namely, Corey, LET and modified Corey, and the corresponding representations of $p_C(S_w)$. Since the data set refers to a primary drainage process, the water endpoint relative permeability is fixed to $k_{rw}(S_w = 1) = 1$. All the other parameters are left open. The residual water saturation is, however, a history matching parameter common for both $k_r(S_w)$ and $p_C(S_w)$ but matched separately from each other. This means that

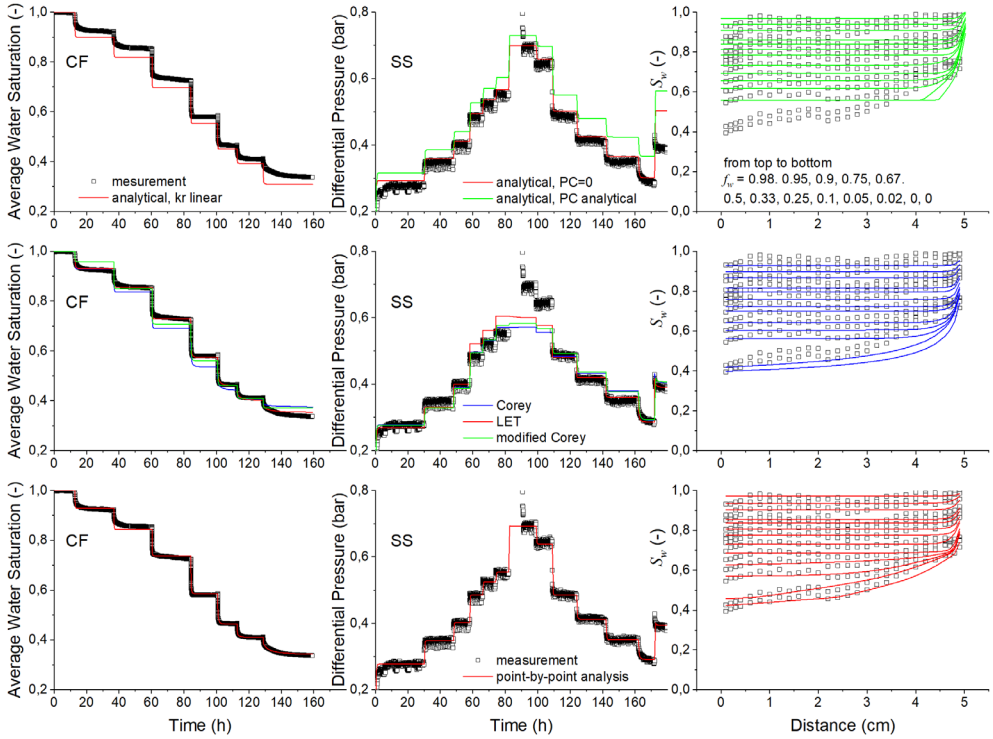

Figure 4 : Experimental data and analytical/numerical interpretations: CF average water saturation (left), SS differential pressure (middle), and SS saturation profiles (right). Top row: forward simulations using the analytical solutions. Middle row: automated and simultaneous history march using different $k_r(S_w)$ power-law input functions in combination with their corresponding $p_C(S_w)$ representations. Lower row: best match using the point-by-point approach.

6.1 Finding Solutions

The analytical solutions using Darcy's law for SS and the Hassler–Brunner equations for CF experiments are shown in Figure 5 and are used as starting points for the numerical simulations. The quality of the analytical solutions is demonstrated by forward simulations and comparison of the results to the experimental data, as shown in the top row of Figure 4. The comparison of the SS differential pressure shows a reasonable match as capillary pressure is ignored. Including the Hassler–Brunner analytical solution in the forward simulation of the SS experiment, the data are no longer matched but rather an overestimation of the differential pressure. The Hassler–Brunner analytical solution itself underestimates the average water saturation of the CF experiment. The observed mismatches emphasize the importance of including both data sets in the analysis and even the importance of simultaneous history matching of $k_r(S_w)$ and $p_C(S_w)$, matching SS and CF experiments simultaneously.

S_{wc} can principally be different for both types of data sets. The starting point of the history match is the analytical solution shown in Figure 5.

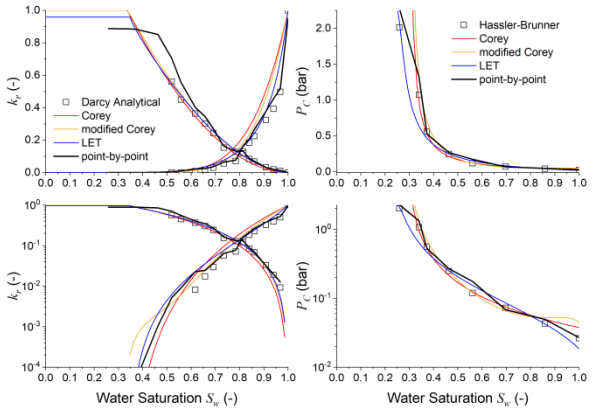

Figure 5 : Analytical solutions (symbols) and results of the history matching using various representations of $k_r(S_w)$ and $p_C(S_w)$, as indicated in the legends. Top: saturation functions on a linear scale. Bottom: the same functions on a logarithmic scale.

As shown in Figure 4, none of these models suitably describe the experimental data sets. Referring to the SS differential pressure, the deviation is strongest close to the crossing points of relative permeability, where the total fluid mobility is lowest, i.e., highest differential pressure values. However, referring to the combined data set of SS and CF, the overall deviations are unacceptable.

With the point-by-point HM approach, we give the system much more degrees of freedom. In this approach we used 17 points for water relative permeability, 17 for oil relative permeability and 8 points for the capillary pressure table. The points for the relative permeability tables are coming from the average of the saturation profiles at each fractional flow until the minimum water saturation measured in the SS experiment. Below this water saturation we get the points from average water saturations of the CF experiment. For the capillary pressure table, we get the points from the average water saturation of the CF experiment. Here we only vary the functional values and the saturation values are constant. The lower row of Figure 4 shows the resulting simulated versus experimental responses. With point-by-point matching, the $k_r(S_w)$ and $p_C(S_w)$ line shapes are not restricted to follow a certain functionality, and with this, complex rock structures may be described. In the present case of Estaillades limestone, all responses can be well described, including the SS saturation profiles for all $f_w(S_w)$. The resulting $k_r(S_w)$ and $p_C(S_w)$ are shown in Figure 5, in which all solutions are compared. The point-by-point approach delivers rather unregularly shaped saturation functions but closely follows the irregularities directly observed in the experimental responses. Furthermore, all resulting saturation functions from the HM of the experimental measurements with the simulation predictions are within rather narrow intervals, which is surprising, considering the quality of the matched versus experimental responses. This opens up the important question about the uncertainty in the procedure and finally the resulting uncertainty in the saturation functions.

The results of the HM simulations depend on the optimization algorithm being used and for the point-by-point approach presented here we found the active-set algorithm in MATLAB *fmincon* function to be the most efficient. The Levenberg-Marqardt (LM) method which is used in the literature [9, 21] does not allow the implementation of inequalities (equation (3)) which is an integral part of the point-by-point approach to force the monotonic behavior for the saturation functions. Other algorithms e.g. interior-point can sometimes lead to a closer match to the experimental measurements in case power law representation for saturation functions are used.

6.2 Uncertainty Analysis

To quantify the uncertainties, we run Monte Carlo simulations using ParaMonte. We specify a chain size of 20,000, which is the number of unique points to be sampled from the likelihood estimation function. For this case it leads to ~1,5 million total likelihood estimation function calls or ~1.5% acceptance rate for the MCMC algorithm. Considering the high-dimensional parameter space, the uncertainty analysis requires a large computational effort resulting in approximately a week of computational time on the used computer system. Figure 6 top shows the value of the likelihood estimation function, which reduces in the early iterations and then oscillates around a value of -15. The adaptation measure is a real number between 0 and 1 with 0 implying no proposal adaptation and 1 implying extreme adaptation. The convergence of the adaptive Markov chain – the type of MCMC simulations that we are using in this study - to the target density is guaranteed, as long as the adaptation of the Markov chain monotonically decreases throughout the simulation. It is, therefore, important to monitor the amount of adaptation in ParaDRAM simulations to ensure the adaptation of the proposal distribution diminishes progressively throughout the simulation [28]. This value is shown in Figure 6 bottom and the moving average is shown to be monotonically decreasing. This is a healthy sign for the implemented Monte Carlo simulation, which shows a convergence in both the sampled likelihood estimation function and input parameters [17]. For the samples used in this study the point-by-point approach showed the best convergence and match with experimental data whereas; the power-law-like saturation functions do not well match the experimental data, which leads to convergence problems of the Monte Carlo simulation. In that case, the tracer chains overshoot to high values, making the uncertainty range larger. This behavior is sample specific and the saturation functions can be predicted using power law function with a high confidence level as shown in the literature [21].

Figure 7 shows the histograms of the simulated k_{ro} (a), k_{rw} (b), and p_C (c) points along the water saturation axis. These histograms can be used to quantify the uncertainty, which may be defined by calculating the P10 to P90 interval given in Figure 8. The interval refers to the probability of 10 to 90% that the quantity—in this case the fluid relative permeability—exceeds the given value. The P50, given in the same panel, refers to a best match from the Monte Carlo approach. In addition, Figure 7 shows the MCMC chain plots (the accepted Markov chain) at selected saturations along with the correlations between neighboring saturation points exemplarily for k_{ro}. The histograms and the MC line tracers show nearly Gaussian distributions except for the endpoint at connate water saturation. This means that the modeled drainage process is less sensitive to the endpoint, reflected in the elongated histogram shape. This leads to the large uncertainty range at the tail of the water relative permeability in Figure 8 (a). The same is true for the capillary pressure (c), as the centrifuge multistep simulation is less sensitive to the capillary pressure at residual water saturation, leading to a larger uncertainty at S_{wc}.

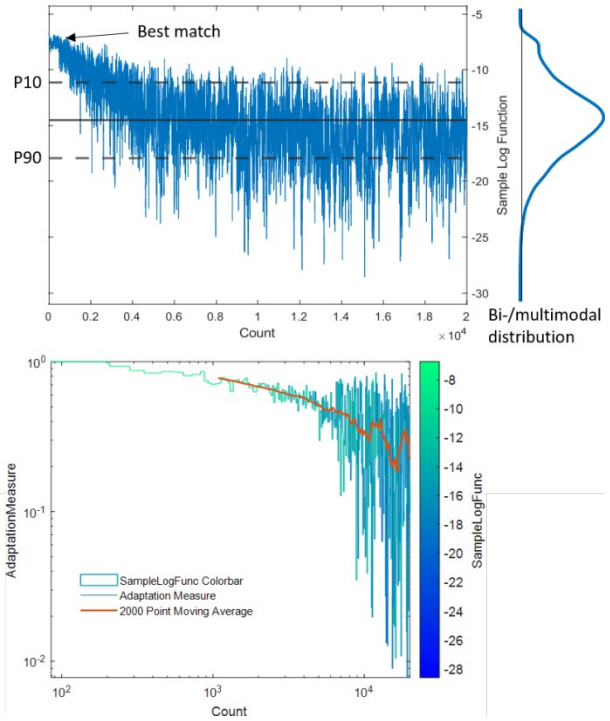

Figure 6: Top: the value of the sampled likelihood estimation function (equation (4)) during the MCMC for the accepted chain of samples. Bottom: the adaptation measure for the full Markov chain.

Although the histograms mostly show Gaussian behavior, the tracer in some chain plots does not always oscillate around a constant value (e.g., $k_{ro}(S_w = 0.97)$). Longer period temporary deviations may be caused by the relatively large parameter space and the respective degrees of freedom, in which the values of some parameters can deviate from the general trend and still be accepted. However, then because of the increased error in the likelihood estimation function, the rejection rate increases, and the chain returns to the previous trend that it was following before.

Figure 8 shows all relative permeability and capillary pressure curves calculated for the Estaillades experimental data sets. It also shows the P10 and P90 range calculated from the earlier discussed data set referring to the histograms in Figure 7. The best history match lies within this range. However, it does not lie on the median of the interval. By performing a forward simulation of the experimental response in the boundary of the P10-to-P90 interval, the P10 and P90 pressure ranges are obtained, as shown in the inset of Figure 8(a). The measured pressure is well within the uncertainty range except around the highest-pressure points (lowest total fluid mobility) and around the pressure of the bump flood. These parts of the pressure plot are close to the boundaries of the calculated range.

The range here corresponds to the fixed relative error that we decided in the beginning before running the MCMC simulations. The resulting uncertainty range around the pressure is higher than the assigned 2.5%, since we also allocate 1% error to the saturation profile and 1% error to the average water saturation from the centrifuge experiment. Depending on the standard deviation of the experimental measurements, the error assigned to the measurements in the equation (4) varies, which affects the calculated uncertainty range.

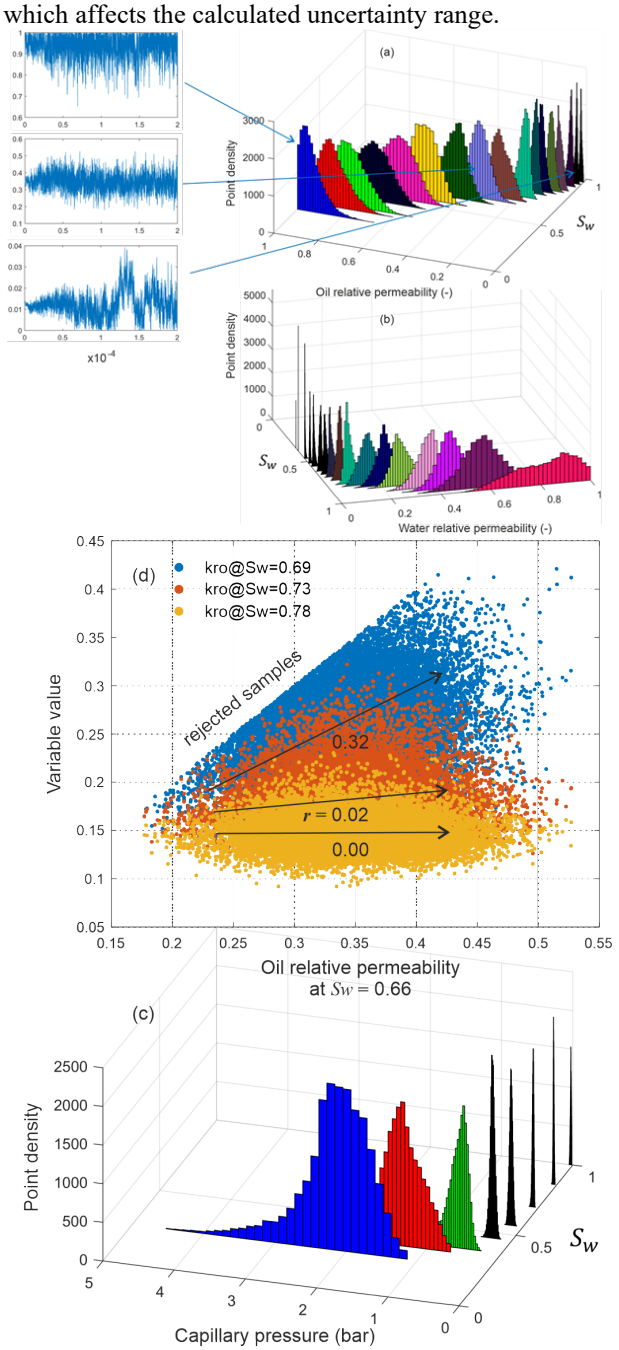

Figure 7: Histograms providing single parameter uncertainties of oil and water relative permeability, (a) and (b), respectively, and capillary pressure (c) saturation functions. MCMC chain plots are exemplarily given for oil relative permeability. (d) Correlation of oil relative permeability at the given water saturation with neighboring saturation points.

The reasoning behind this is intuitive since by doing so, we change the shape of the sampled response surface. The Pearson correlation matrix and the full grid plots for this analysis show the correlation strength between the history matched parameters. The map shows strong correlations between neighboring saturation points. This is partly caused by the forced monotonic behavior that we apply to our simulations. The relative permeability table shows positive correlation between the water saturation points next to each other (Figure 7 (d)) and this correlation is

negative for the capillary pressure table. At lower water saturations, the positive correlation between k_r saturation points span several next neighbors, which is the reason for the larger uncertainty interval at low S_w. At higher water saturations, there is a negative correlation between the water and oil relative permeability. This means that at higher water saturations, the total mobility (relative permeability at constant viscosity) is split between oil and water; as phase mobility increases, the mobility of the complimentary phase decreases—a behavior that we physically expect.

Figure 7 (d) illustrates the correlation strength between k_{ro} at $S_w = 0.66$ and its neighboring points. The Pearson's correlation strength r is labeled in the plot below the black arrows. This demonstrates that with increasing water saturation, the correlation vanishes.

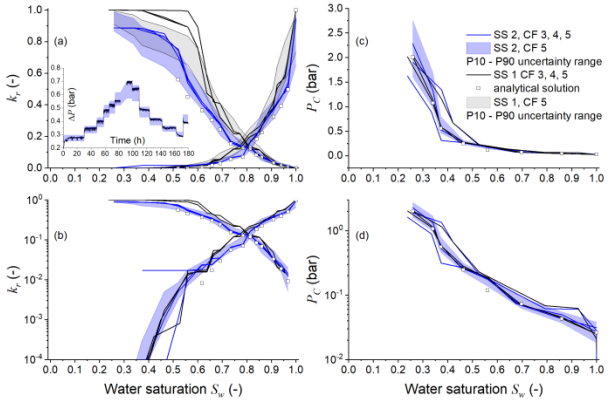

Figure 8: Panel (a) and (b): resulting relative permeability on a linear and logarithmic scale from experiment/sample SS 2 in combination with CF 2, 3 and 5. The uncertainty range is given for the combination SS2, CF 5. For comparison, the pair-wise analysis of SS1 with CF 3, 4 and 5 is given as well. Panel (c) and (d) provide the same information, but for the capillary pressure. The inset in (a) shows the P10 to P90 uncertainty interval for the differential pressure response during the SS 2 experiment as an example.

6.3 Sample-to-Sample Variation

It is a common problem that carbonates often show heterogeneity on various scales. In SCAL, we typically ignore heterogeneity on the plug scale, and SCAL data are numerically interpreted by assuming a simulation domain with homogeneous rock properties. However, sample-to-sample variations are common, even if the samples are drilled from locations close to each other. Therefore, it should be common practice to measure saturation functions on more than one plug from the region. In the present study on Estiallades, which is a common outcrop rock, the samples are from the same block and are therefore "twin plugs". A natural question is whether measurements on twin plugs deliver results within the uncertainty range of the individual data set. [21] proposed a method to deal with the common data interpretation problems that rises from the heterogeneities of samples in SCAL experiments. They argued that by calculating the variability number (V) of the plugs using the X-Ray measurements one can decide on the significance of the heterogeneity based on the cut-off value for V. Their approach warrants further work to be looked into, also in the framework of the reliability of the analysis provided from a small number of samples, in the future.

What we deliver in this study is an indication only because 5 plugs (a common number of samples available for SCAL) and 2 and 3 repeat measurements may or may not provide a solid statistical basis [21]. However, we use the two SS and the three CF experiments from [18] and simultaneously analyze all possible SS and CF combinations. The results are shown in Figure 8 (a) and (b) for relative permeability and (c) and (d) for capillary pressure. The simultaneous analysis shows a strong deviation between the SS results but a relatively small influence of the sample-to-sample variation in the CF experiments; the resulting curves split into two groups referring to the two SS experiments, which differ predominantly in the oil branch toward low water saturations, where the strongest point-to-point correlations are found as will be discussed further below. With respect to uncertainty, for simulations with a given SS data set, the k_r curves generated by combining with the different CF data lie within a narrow window compatible with the individual uncertainty range from MCMC. However, the two groups do not fall into the individual uncertainty ranges but show a certain overlap over the whole saturation range. In this specific case, it appears that sample-to-sample variation plays a stronger role than the uncertainty coming from individual data sets and their combinations.

6.4 Results: Bimodal Distributions

The samples from the likelihood estimation function shown at the top of Figure 6 show a rather multimodal histogram, indicating that there is no unique solution in the error surface. Figure 9 shows the histograms of $k_{ro}(S_w)$ for the SS 1/CF 5 case, where the best match lies partly outside the P10-P90 interval; in (c), the histograms are bimodal for water saturations below 0.6 and above 0.95, with a pronounced narrow maximum and an overlapping broad component. The global minimum is found using the MATLAB *fmincon* function—the best match, while the broad component dominates the uncertainty range in the MCMC sampling. Using equation (4) as the objective function in the *fmincon* function (without the -1/2 factor) leads to comparable results and trends when the *fmincon* function is used with equation (3) (see section 4.1), which excludes the influence of the specific choice of the objective function.

The complex bimodal histograms may be related to the following aspects: (a) At low S_w, the dataset is outside the range of the SS experiments. The information regarding k_r therefore comes exclusively from the centrifuge experiments. (b) Especially in the SS1 case, the HM result for k_{ro} is closely tied to 1 in this saturation range. If a monotonic behavior with $k_r \leq 1$ is required, most of the samples are rejected during HM in the respective range.

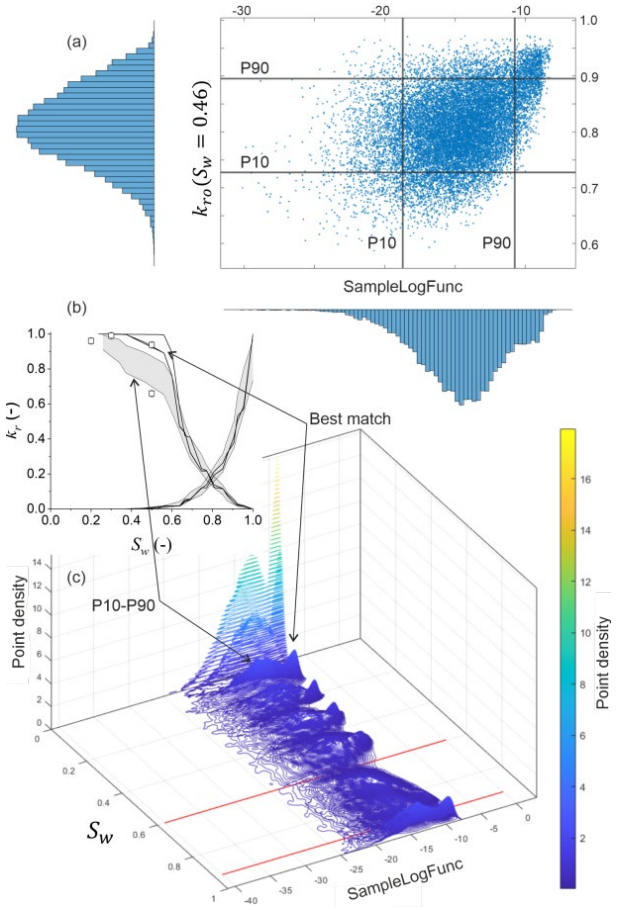

Figure 9: Sampled likelihood estimation function (equation (4)) versus oil relative permeability for the SS1 and CF5 combination. (a) for a single saturation state, S_w = 0.46; (c) for the full range of S_w. (b) Relative permeability and uncertainty interval from *Figure 8* for comparison. The white symbols represent results from porous plate experiments, with errors of individual measurements in the order of the symbol size.

The symbols in Figure 9 (b) show the results of porous plate (PP) experiments [18]. By means of the PP method, samples are desaturated to a certain water saturation close to S_{wc}. Subsequently, the effective permeability is measured by multi-rate decane flooding (at $f_w = 0$). Assuming that the aqueous phase is largely immobile, k_{ro} was derived. However, also with the additional PP data, it is not possible to decide on the true k_{ro}. Due the sample-to-sample variation—considering that the PP experiments were performed on different samples—the derived k_{ro} values vary in the full spread of generated data.

7. Summary and Conclusions

In the present study, we present a comprehensive way to interpret SCAL data. We apply a workflow starting from the well-known analytical solutions, directly derived from the individual data sets, as input for numerical history matching. The experimental data sets are described simultaneously and by means of a point-by-point parameterization - 34 points for the two relative permeability tables combined and 8 points for the capillary pressure table. With these innovations, a good description of complex saturation functions is possible.

Different parametrizations of the saturation functions are used. The study shows that using classic power-law representations is not sufficient to conclusively analyze data derived from more complex rock types, such as microscopically heterogeneous carbonates. For this purpose, the point-by-point approach, in which the saturation functions were evaluated at the individual saturation points defined by the experimental steps that serve as HM parameters. This approach allows us to match complex rocks since the functions are not restricted to power laws.

Furthermore, the simultaneous evaluation of SS and CF experimental data sets accounts for the fact that k_r and p_C are coupled. The results show that simultaneous rather than subsequent evaluation of those data sets leads to more objective results. With "objective" we mean to prefer a solution without manual, respectively personal intervention in the process. However, the massive increase in the free parameters in the simultaneous point-by-point approach substantially increases the required computational power, especially in cases where uncertainty analyses are performed.

The uncertainties are evaluated by MCMC simulations sampling the response surface of the likelihood estimation function of the combined data set. This allows the extraction of single parameter distribution functions and correlations between those parameters on the saturation scale. The study shows that despite the given high degree of freedom, the simultaneous point-by-point approach delivers a very robust description of two-phase flow in complex rock types. While the gradient-based HM reliably finds the best match, MCMC sampling demonstrates the complexity of the response surface. This results in one SS data set for a separation of the best match and the P10-P90 uncertainty interval (the best match is within the P01-P99).

By combining all available SS and CF experimental results for analysis, a comparison of the sample-to-sample variation with respect to the error of the individual data set could be made. For the specific rock type, the sample-to-sample variation seems to be dominant (as far as the limited data set allows for that statement). The results group around the individual SS curves with a narrow bandwidth by the various CF measurements. The P10-to-P90 uncertainty intervals of the two SS curves just marginally overlap apart from the saturation range around S_{wc}; the individual data sets also show the greatest uncertainty around S_{wc}, which may have to do with the missing next-neighbor information toward lower water saturations.

The authors acknowledge valuable discussions with Jos Maas, Steffen Berg and Pit Arnold.

References

[1] M. C. Leverett, "Capillary Behavior in Porous Solids," *Transactions of the AIME,* vol. 142, no. 01, p. 152–169, 1941.

[2] D. D. Huang and M. M. Honarpour, "Capillary end effects in coreflood calculations," *Journal of*

Petroleum Science and Engineering, vol. 19, no. 1-2, p. 103–117, 1998.

[3] E. Johnson, D. Bossler and V. N. Bossler, "Calculation of Relative Permeability from Displacement Experiments," *Transactions of the AIME,* vol. 216, no. 01, pp. 370-372, 1959.

[4] G. L. Hassler and E. Brunner, "Measurement of Capillary Pressures in Small Core Samples," *Transactions of the AIME,* vol. 160, no. 01, p. 114–123, 1945.

[5] J. Hagoort, "Oil Recovery by Gravity Drainage," *Society of Petroleum Engineers Journal,* vol. 20, no. 03, p. 139–150, 1980.

[6] J. G. Maas and A. M. Schulte, "Computer simulation of Special Core Analysis (SCAL) flow experiments shared on the Internet," 1997.

[7] J. G. Maas, B. Flemisch and A. Hebing, "Open Source Simulator for DuMux Available for SCAL Data Interpretation," p. 18–21, 2011.

[8] D. Loeve, F. Wilschut, R. H. Hanea, J. Maas, P. Hooff, P. van den Hoek, S. G. Douma and J. Doren, "Simultaneous Determination of Relative Permeability and Capillary Pressure Curves by Assisted History Matching Several SCAL Experiments," *Society of Core Analysis Conference Paper SCA2011-35,* 2011.

[9] S. Berg, E. Unsal and H. Dijk, "Non-uniqueness and uncertainty quantification of relative permeability measurements by inverse modelling," *Computers and Geotechnics,* vol. 132, p. 103964, 2021.

[10] M. Rücker, A. Georgiadis, R. T. Armstrong, H. Ott, N. Brussee, H. van der Linde, L. Simon, F. Enzmann, M. Kersten and S. Berg, "The Origin of Non-thermal Fluctuations in Multiphase Flow in Porous Media," *Frontiers in Water,* vol. 3, 2021.

[11] S. Berg, E. Unsal and H. Dijk, "Sensitivity and Uncertainty Analysis for Parameterization of Multiphase Flow Models," *Transport in Porous Media,* 2021.

[12] R. H. Brooks and A. T. Corey, "Hydraulic Properties of Porous Media," no. 3, 1964.

[13] A. T. Corey, "The interrelation between gas and oil relative permeabilities," p. 38–41, 1954.

[14] F. Lomeland, E. Ebeltoft and W. Thomas, "A New Versatile Relative Permeability Correlation," *Society of Core Analysis Conference Paper SCA2005-32,* 2005.

[15] A. R. Valdez, B. M. Rocha, G. Chapiro and R. Weber dos Santos, "Uncertainty quantification and sensitivity analysis for relative permeability models of two-phase flow in porous media," *Journal of Petroleum Science and Engineering,* vol. 192, p. 107297, 2020.

[16] K.-A. Lie, An Introduction to Reservoir Simulation Using MATLAB/GNU Octave, Cambridge University Press, 2019.

[17] A. Shahmoradi and F. Bagheri, ParaDRAM: A Cross-Language Toolbox for Parallel High-Performance Delayed-Rejection Adaptive Metropolis Markov Chain Monte Carlo Simulations, 2020.

[18] H. Ott, C. H. Pentland and S. Oedai, "CO 2 –brine displacement in heterogeneous carbonates," *International Journal of Greenhouse Gas Control,* vol. 33, p. 135–144, 2015.

[19] S. Krogstad, K. Lie, O. Møyner, H. M. Nilsen, X. Raynaud and B. Skaflestad, "MRST-AD - an Open-Source Framework for Rapid Prototyping and Evaluation of Reservoir Simulation Problems," pp. SPE-173317-MS, 2015.

[20] "Sendra," prores, [Online]. Available: https://www.prores.no/solution/sendra. [Accessed 08 06 2022].

[21] J. G. Maas, N. Springer and A. Hebing, "Defining a sample heterogeneity cut-off value to obtain representative Special Core Analysis (SCAL) measurements," *Society of Core Analysts,* 2019.

[22] S. Berg, E. Unsal and H. Dijk, "Impact of Relative Permeability Parameterization on the Uncertainty of Multiphase Flow Models," 2020.

[23] S. Kumbhare and A. Shahmoradi, *MatDRAM: A pure-MATLAB Delayed-Rejection Adaptive Metropolis-Hastings Markov Chain Monte Carlo Sampler.*

[24] MathWorks, MATLAB optimization toolbox user's guide, R2020b ed., 2020.

[25] R. Lenormand, K. Lorentzen, J. G. Maas and D. Ruth, "Comparison of Four Numerical Simulators for SCAL Experiments," *Petrophysics - The SPWLA Journal of Formation Evaluation and Reservoir Description,* vol. 58, no. 01, p. 48–56, 2017.

[26] S. M. Skjaeveland, L. M. Siqveland, A. Kjosavik, W. H. Thomas and G. A. Virnovsky, "Capillary Pressure Correlation for Mixed-Wet Reservoirs," *SPE Reservoir Evaluation & Engineering,* vol. 3, no. 01, p. 60–67, 2000.

[27] K. Pearson, "Notes on regression and inheritance in the case of two parents," *Proceedings of the Royal Society of London,* no. 58, pp. 240-242, 1895.

[28] A. Shahmoradi, F. Bagheri and J. A. Osborne, "Fast fully-reproducible serial/parallel Monte Carlo and MCMC simulations and visualizations via ParaMonte:: Python library," *arXiv preprint arXiv:2010.00724,* 2020.